$Nb_yW_{1-y}O_z$ and $Nb_xTi_{1-x}O_z$ pseudobinaries as anodes for Li-ion batteries

Sarish Rehman†, J. Michael Sieffert†, Christopher J. Lang and Eric McCalla*

Department of Chemistry, McGill University, Montreal, Canada

† Contributed equally.

* Corresponding author: eric.mccalla@mcgill.ca

Abstract:

Although high energy density Li-ion batteries are a high priority for electric vehicles, there is also an important demand for safe high power batteries for various applications including medical devices. In such applications, the state-of-the-art anode is $Li_4Ti_5O_{12}$ (LTO) with limited capacities. Herein, we utilize a high-throughput approach to study compositions of Nb-based anodes in two pseudobinary systems: $Nb_yW_{1-y}O_z$ and $Nb_xTi_{1-x}O_z$ as potential high capacity replacements for LTO. All samples are characterized by both X-ray diffraction and electrochemistry in high-throughput. The resulting phase stabilities are presented and show significant solid solution regions that have never been explored before. The resulting electrochemical data show that numerous compositions (particularly for Nb metal fraction above 50%) show excellent performance with capacities over 200 mAh/g, very good rate performance (e.g. >80% capacities when the CV sweep rate is increased by an order of magnitude) and diffusion constants greater than 10^{-6} cm^2 s^{-1} in high loading electrodes (about 20 mg/cm^2). This study represents a first precise screening of battery performance across these two binaries of high current interest and permits a deepening of our understanding of the structure-property relations in these important systems.

1. Introduction:

The growing global energy demand of lithium-ion batteries (LIBs) with high energy density and high rate performance is being driven by the ever-increasing need for energy on a worldwide scale as well as the quest for alternative energy sources that are clean and renewable.[1,2] Although such high energy density batteries are badly needed, it is important to note that there are also a number of applications demanding new high-power electrode materials that can store large quantities of charge and transfer that charge in a few minutes rather than several hours.[3,4] Such materials can enable the development of new power-intensive devices. Generally, the state-of-the-art for high power Li-ion batteries depends on electrodes where particles are nanoscaled or rely on complex hierarchical porous structures.[5,6] Such techniques are effectively used in $LiFePO_4$ cathodes, for example, and reduce Li^+ solid-state diffusion lengths (rather than improve the diffusion coefficient). However, nanoscaling or nanostructuring can have disadvantages particularly in materials operating near the limits of the stability window of the electrolyte. In such cases the high surface area may result in severe electrolyte degradation.[7–9]

On the anode side, graphite is the most common commercially used material for high energy applications. However, it is not suitable for usage at high rates because of particle fracture and the likelihood of Li dendrite growth, which can cause short circuits and even fires and explosions.[10,11] Nanosizing graphite certainly is not recommended, given that it has electrolyte stability issues at low voltages resulting in the formation of a passivating layer known as surface electrolyte interphase (SEI) layer.[12] This layer consumes Li^+ during formation, lowering the initial coulombic efficiency of the cell.[13] Moreover, the formation of dendrites negatively impact the cycle life, rate capability and safety of the cell. Therefore, in applications where safety is of utmost concern such as numerous medical devices, graphite is to be avoided and anodes operating at higher voltage

(*e.g.* $Li_4Ti_5O_{12}$) have proven to yield extremely safe and long lasting batteries in fact achieving long-term cycling performance never achieved by graphite cells.[14,15] $Li_4Ti_5O_{12}$ (LTO) is also considered to be a good candidate for high power applications due to its near zero-volume expansion during cycling which permits a high rate of Li cycling, and operation at an elevated voltage of 1.55 V implies no risk of SEI formation/cracking, nor dendrite growth.[16,17] Despite the decrease in energy density due to the higher operating voltage, LTO anodes have clearly met a demand in important safety and/or power driven applications.[14,15] However, LTO has issues related with the evolution of H_2 and CO_2 gases during cycling and has a limited specific capacity of 175 mAh/g.[18–22] Clearly, high power anode materials are required for safe Li-ion cells with high power densities, but continued efforts are required to further improve the energy density.

Recently, niobium-based pseudobinary oxides including $TiNb_2O_7$, $Nb_{14}W_3O_{44}$ and $Nb_{16}W_5O_{55}$ have been identified as being very promising.[3,23,24] These materials show higher capacities than LTO at a comparable potential. These studies utilized traditional solid-state synthesis methods and extremely high synthesis temperatures exceeding 1300 ºC. However, to understand the complex relationship between metal compositions, structures, and the resulting battery properties there is a need for systematic study across the entire binaries to explore wide composition ranges in order to improve the properties of these promising materials. Although the phase diagrams of both pseudobinary systems (Nb-W-O and Nb-Ti-O) at these elevated temperatures have long been known[25–27], no attempt has been made to probe the electrochemistry across the entire systems, nor have studies looked at lower sintering temperatures.

Herein, we utilize a high throughput (HTP) system to investigate the relationships between chemical compositions, crystal structures, and electrochemical properties. We utilize HTP methods developed by our group previously[28–30] to make high-quality $Nb_yW_{1-y}O_z$ and $Nb_xTi_{1-x}O_z$

materials on the 5 mg scale and perform both structural and electrochemical analysis across the entire pseudobinary systems.

2. Experimental methods:

HTP approaches have been utilized for all synthesis and characterization. First, a sol–gel method was adopted for the synthesis to achieve samples of both full binaries, as described in detail in ref.[28] Specifically, the samples were made by first dispensing volumes of 0.8 M WO_3, titanium butoxide, and ammonium niobate oxalate hydrate into alumina cups. These volumes varied for each step by maintaining 64μL of combined precursors for each cup. By stepping 1μL in volume in each direction with each new sample, the entire set of pseudobinaries were synthesized. The titanium butoxide and ammonium niobate oxalate hydrate were made by adding reagents to EtOH and water, respectively. The WO_3 precursor was made by boiling the WO_3 reagent in a 1:1 mixture of water and NH_4OH and adding water to the desired dilution after dissolution of the reagent. Two sets of 64 samples are prepared with compositions: (i) $Nb_yW_{1-y}O_z$ with y = 0, 1/63, 2/63, …, 1 and (ii) $Nb_xTi_{1-x}O_z$ with x = 0, 1/63, 2/63, …, 1. Note: z here is left as a variable out of caution, but it is likely to be a function of x and y only given that Nb, W and Ti each typically take one oxidation state only under our synthesis conditions. This represents 127 unique compositions (Nb_2O_5 being the x = 1 and y = 1 samples). It is important to note that the difference in composition between neighboring samples ($\Delta x,y = 0.0167$) represents a change of only 1 μL in the dispensed volumes. This was found to be too small and resulted in noise in both the XRD and the electrochemical data which was rectified by binning the data in each binary into 32 bins of 2 compositions each. As such, we conclude that the smallest step size we can reliably resolve by our HTP methods is 2 μL (this is the first study where we attempted a smaller step size). Citric acid (3 M) was then added as a chelating agent. These homogenous precursor solutions then underwent a gelation process by

heating at 60 °C, 110 °C, and 200 °C under vacuum. The resulting gels were crushed and positioned in an 8 × 8 aluminum smokestack to prevent sample cross-contamination while off-gassing occurred when heated at 400 °C for 6 h to remove nitrate and citrate bi-products formed in the gelation process. After removing the smokestack, the samples were further calcinated at 1000 °C for 3 h in ambient air (heating at 10 °C min^{-1} and cooling at 5 °C min^{-1}). These calcination conditions were selected to prevent W sublimation which can be a significant problem at high temperatures while still yield highly crystalline products.

All samples were first characterized using high-throughput X-ray diffraction (XRD). The XRD measurements were performed in transmission mode using a Panalytical Empyrean diffractometer with a Mo target (60 kV, 40 mA) and a GalaPIX area detector. For Mo Kα radiation (λ = 0.70926 Å for Kα1), a scattering angle range of 4 – 30° was selected (this corresponds to approximately 10–70° for Cu radiation). For all samples, the main peak intensity was well over 1000 counts for the 10 min scans, demonstrating that the data has a high signal to noise ratio. It is worth noting that backgrounds here are as high as 10 % of our peaks, far larger than in our previous studies with this XRD instrument, and this is attributed to Nb fluorescing under Mo-radiation (similar to the effect seen with some 3d metals with Cu radiation). Each scan took <10 min and an entire batch of 64 samples could therefore be characterized in <10 h. For ease of comparison to the rest of the literature, all patterns have had the Mo-Kα2 peaks stripped, and scattering angles have been converted to those that would be obtained with Cu-Kα1 radiation (λ = 1.54051 Å) as described in detail in ref.[28] Pawley fits were performed on all single-phase patterns.

After XRD, a portion of each sample was then utilized for electrochemical testing. Both a high loading (about 20 mg/cm^2) and low loading (about 2.5 mg/cm^2) method were used for electrode fabrication (in part to compare these two methods and quantitatively determine the rate

performance of these materials in high loading electrodes). Combinatorial cells with an 8 × 8 array of electrode were used to test electrochemical properties as described in detail in ref.[31] Firstly, a custom-designed printed circuit board (PCB, Optima Tech) with 64 Ni pads was used. Two different electrode loadings were utilized. The first, referred to as high loading here, involved composite electrodes with 2 mg of active material (AM) and approximately 20 wt% carbon black and 20 wt% polyvinylidene fluoride (PVDF), both of which were added by drop-casting an *N*-methyl-2-pyrrolidone (NMP) solution onto the AM powders.[29] This yields electrodes with an active material (AM) loading of approximately 20 mg/cm^2. In the second method, called low loading, a slurry comprising of 85 wt% AM, 10 wt% carbon black and 5 wt% of PVDF in NMP was prepared by stirring with a stir bar, then 4µL of the slurry was drop cast onto a Ni pad, yielding an electrode with approximately 0.3 mg of AM as described in ref.[30,32]. This yields a mass loading of approximately 2.5 mg/cm^2. One objective is to determine if these two methods yield equivalent electrochemistry or if the transport through the Nb-based materials becomes limiting in the thicker electrodes. For either loading, the PCB and electrodes were dried at 65 °C overnight to evaporate the NMP. The assembly of the combinatorial cell was performed in an argon-filled glovebox. The electrolyte was 1 M $LiPF_6$ in 1:1 EC: DMC (SoulBrain MI). Li metal foil was used as the counter electrode with two Whatman GF/D glass microfiber separators. The cell was then sealed using a 3M double-sided sealing tape as described in ref.[29] Cyclic voltammetry (CV) was performed with the voltage range 1.0 to 3.0 V *vs.* Li/Li$^+$ on a lab-built HTP electrochemical system described in refs. [28,33,34], which utilizes a quad voltage source (Keithley 213) and a Keithley 2750 multichannel voltmeter. 64 CVs were performed simultaneously. Data were processed to extract average voltages, and specific capacities over the multiple cycles performed. For the cycling experiments, a single protocol was designed for the extraction of many electrochemical parameters. This

protocol, shown in Fig. 1, included a set of cycles at different sweep rates ranging from 0.1 V h^{-1} to 2 V h^{-1} followed by 10 cycles at a rate of 0.1 V h^{-1} for the analysis of the materials' extended cycling. This protocol allowed for the determination of numerous relevant electrochemical properties of 64 samples at one time.

3 Results and Discussion:

3.1 X-ray diffraction

Figures 2 and 3 show XRD results obtained for 32 representative $Nb_yW_{1-y}O_z$ and 32 $Nb_xTi_{1-x}O_z$ materials, respectively, all synthesized at 1000 °C. It should be noted that z is not a free variable here, it is a function of x (or y) and the oxidation states of each of Nb, W and Ti. It is of high interest that despite the modest temperatures used compared to previous literature, the XRD patterns show excellent crystallinity with a high number of phase pure materials as expected from the previously published phase diagrams.[25,27] It should be emphasized that previous phase diagrams were generally at much higher temperatures (the Nb-Ti-O system has no data at 1000 °C, while the Nb-W-O has 4 data points in previous studies). The phase stabilities were extracted from the XRD patterns. Solid solution regions are shown in Figure 4 as colored rectangles and co-existence is shown with a white background.

We now consider the progression of XRD patterns systematically in Figure 2. The $Nb_yW_{1-y}O_z$ system contains five stable phases which are expected at y = 0 (WO_3), 0.39 ($Nb_{13.5}W_{20,5}O_{94}$), 0.67 (Nb_2WO_8), 0.82 ($Nb_{14}W_3O_{44}$) and 1 (Nb_2O_5). All samples made at these compositions here show these as pure phases, but as discussed below, 3 of these phases exist as solid solution regions with more than 1 composition taking the structure. The y = 0 endmember shows pure phase WO_3 as expected with a high quality fit obtained in Figure 5 and lattice parameters in good agreement with the literature in as shown in Table I. The next sample (y = 0.031) already shows additional peaks

compared to WO_3 and phase coexistence persists until y = 0.349 where phase pure $Nb_{13.5}W_{20.5}O_{94}$ is obtained. From this point all the way to y = 0.666, phase pure materials are obtained. This solid solution region is in agreement with the results first reported by Goldschmidt[35] on the Nb_2O_5–WO_3 system and he came to the conclusion that the solid solution extends up to 50 mole percent WO_3 (y = 0.666) in solid solution. Table I shows some minor variation in lattice parameters throughout the solid solution, but there is no trend with composition and no large variation. We attribute this to the similar ionic radii of W^{6+} in VI coordination (0.60 Å) and Nb^{5+} (0.64 Å), so very little changes in lattice parameters with substitutions is expected (note: Ti^{4+} is also very close with 0.605 Å). As we progress to higher y values, we transition to another solid solution Nb_2WO_8 as shown in Figure 2. This region is followed by a solid solution region of $Nb_{14}W_3O_{44}$ and then a co-existence region of $Nb_{14}W_3O_{44}$ and Nb_2O_5. Finally, a solid solution of Nb_2O_5 exists at the highest Nb contents and this agrees well with litertature.[36,37] Again for all phases here, the fits in Figure 4 are excellent and lattice parameters at the stoichiometric compositions are in good agreement with the literature. The stability relations of the various reported polymorphs of Nb_2O_5 have been reported by several researchers.[38,39] It has been determined that only high-temperature monoclinic Nb_2O_5 is stable at atmospheric pressure. Gatehouse and Wadsley described the high-temperature modification of Nb_2O_5 to be monoclinic with lattice parameters in good agreement with our results as shown in Table I.[40] It is highly noteworthy that quite large solid-solution regions are obtained with high crystallinity in the Nb-W-O, particularly when keeping in mind that other studies perform their syntheses at least 300 °C higher than that reported here.

Figure 3 shows the progression of the XRD patterns along the $Nb_xTi_{1-x}O_z$ binaries. By contrast with the W containing materials, the materials in this binary show very little solid solution regions. The pseudobinary system contains four stable phases: Nb_2O_5 (x=1), Nb_2TiO_7 (expected at x =

0.666), $Nb_{10}Ti_2O_{29}$ (x = 0.8333) and TiO_2 (x = 0). All 4 phases are obtained as pure materials here, at the expected composition, except for Nb_2TiO_7 which was found at x = 0. Figure 2 shows the progression of the coexistence regions existing between each as depicted in the phase stabilities in Figure 4. Only the $Nb_{10}Ti_2O_{29}$ phase shows the presence of a solid solution, and only over a narrow composition window. As was the case in the Nb-W-O system, fits in Figure 5 are excellent and lattice parameters match the literature in Table I. This phase stability is in excellent agreement with what we obtain by extrapolating the phase diagram published previously[27] down to our synthesis temperature of 1000 °C. This demonstrates that no phase transformations of note are occurring during the slow cooling used during synthesis. It is also important to recognize that the current study only explores the phases stabilized at the moderate temperature of 1000 °C, there are of course other phases of interest at higher temperatures as explored previously in the literature (*e.g.* ref. [3]).

3.2 Electrochemical Testing

In order to investigate the electrochemical properties of both binaries, HTP cyclic voltammetry was performed on all samples. All samples were cycled between 1.0 and 3.0 V at a series of different rates. Representative voltammograms and voltage curves are shown in Figure 6 for the $Nb_yW_{1-y}O_z$ pseudobinary, displaying increasing electrochemical activity with an increase in Nb content. This can be seen in the growth of the CV peaks which increase in intensity over this composition space. Two principal peaks emerge over the binary in the discharge curves. It has been suggested that the higher voltage peak around 1.9 V corresponds to the Nb^{5+}/Nb^{4+} redox couple, and the peak around 1.4 V corresponds to the Nb^{4+}/ Nb^{3+} redox couple.[41] The relative intensities of these two peaks also implies a relative difference in the redox activities of the material based on their compositions, with the two peaks having similar intensity at lower Nb contents,

while at higher Nb contents the higher voltage peak increases becoming dominant in intensity. The peak of highest intensity is shifted to lower voltages with an increase in Nb content. At y = 0.349 where the $Nb_{13.5}W_{20.5}O_{94}$ phase is found this peak is found around 2.25 V, while at higher Nb compositions this peak is found around 1.9 V, displaying a shift of over 0.3 V, which indicates a change in redox potential as will be evident in the average voltage plots in Figure 4e. The associated voltage curves (Fig. 6e-h) show a stark contrast between the low and high Nb compositions. Materials high in W display modest specific discharge capacities but a high irreversible capacity, while their higher Nb counterparts have specific capacities above 200 mAh/g.

Similar electrochemical trends are found in the voltammograms of the $Nb_xTi_{1-x}O_z$ binary, seen in Figure 7. High Ti compositions are nearly electrochemically inert, while robust redox activity is found at high Nb content once co-existence with Nb_2TiO_7 becomes appreciable. Two discharge peaks are again found in this binary, though the higher voltage peak is more prominent. The lower voltage of the two exists mostly as a shoulder in the higher Ti content materials, though it grows into a more prominent peak at higher Nb compositions. Once again, the voltage curves clearly show that discharge capacity increases and irreversible capacity drops dramatically as the Nb content increases.

The large number of CVs were analyzed to extract average voltages, specific capacities, and peak voltages. Figures 4 and 8 show extracted parameters from the HTP data. Error bars shown on the specific capacities (figures 4ab) are the error on the mean obtained from all replicate samples (note: more replicates were obtained in the high Nb regime (x,y>0.6). In examining these discharge capacities for both binaries, a similar trend emerges. Without Nb the capacities are near zero, upon increasing the amount of Nb the capacities gradually increase until reaching a plateau near 200

mAh/g. This plateau is reached in the $Nb_{13.5}W_{20.5}O_{94}$ solid solution region, and at Nb_2TiO_7 in the $Nb_yW_{1-y}O_z$ and $Nb_xTi_{1-x}O_z$ systems, respectively. These plateaus indicate that beyond a certain Nb content, both binaries produce high-capacity anode materials over extremely wide composition ranges. The $Nb_xTi_{1-x}O_z$ binary features higher capacities, with some compositions possessing capacities of up to 235 mAh/g around x = 0.71, where Nb_2TiO_7 is the predominant phase.

Both binaries feature similar trends in irreversible capacity (Figure 4 c-d). Low Nb compositions feature high degrees of irreversible capacity, as discussed in regards to the representative voltage curves in Figs. 6-7. As Nb content increases, the reversibility of the Li insertion improves. Both systems show a relatively low irreversible capacity of about 10-15 % for samples with at least 50 % Nb.

Average voltages for both binaries also follow a similar trend, a small increase once appreciable discharge capacities are obtained (x,y ≈0.15) followed by a gradual decrease in voltage associated with an increase in Nb content (Figure 4 e-f). In the $Nb_yW_{1-y}O_z$ binary, average voltages range from about 2.3 V for compositions with high W content to about 1.7 V for the high Nb compositions. The $Nb_xTi_{1-x}O_z$ binary sees a milder change in average voltage, with the high Ti content compositions having average voltages around 2.0 V, and high Nb compositions closer to 1.8 V.

Extended cycling analysis was done for the binaries, consisting of ten charge-discharge cycles at a rate of 0.1 V h^{-1} with the retention plotted in Figs. 4 g-h. Of the two, the $Nb_yW_{1-y}O_z$ binary featured more impressive capacity retentions of up to 96.8% for some compositions. Though there does not seem to be a consistent trend for capacity retention over composition in this binary, the compositions of highest capacity retention are found around y = 0.5 representing the $Nb_{13.5}W_{20.5}O_{94}$ phase. The $Nb_xTi_{1-x}O_z$ binary on the other hand displays more consistent retention

over the span of the binary. These values are, however, lower with most compositions being found around 61%. The highest capacity retention in this binary is 68.4%, again much less impressive than the majority of compositions within the $Nb_yW_{1-y}O_z$ binary. It is worth noting that there is a significant difference here between the x=1 and y=1 samples (77 vs. 67 %). Although some of this will result from the average in the two bins as described in the experimental section, but it should also be acknowledge that the Ti data generally shows lower retention. This shows that although trends within a single combinatorial cell are quite meaningful in terms of capacity retention, there can be discrepancies between cells as seen here.

Compared to their discharge capacities at 0.1 V h^{-1}, both binaries showed impressive performance at a faster rate of 1 V h^{-1} (Figure 8 a-b). Neither binary showed significant variation correlated to Nb content with nearly all samples showing high rate capacities between 80-90 % of that obtained at the slower rate. The $Nb_xTi_{1-x}O_z$ binary gave marginally higher rate retention, with some compositions retaining up to 96% of their 0.1 V h^{-1} capacity. The retention in the $Nb_yW_{1-y}O_z$ binary was also satisfactory, as most compositions gave similar values between 85-90%. It should also be noted that the multiple cycles needed for this rate test did not perform well for the samples at high *x* values which is why they were omitted (there may have been damage in that area of the combinatorial cell). The overall excellent rate performance again illustrates that Nb-based anodes are ideal for high power applications and that the lower synthesis temperatures used here do not hinder this. Again, the high performance is seen over wide composition windows.

Analysis of both binaries Li^+ diffusions coefficients was also performed using CV data from multiple cycles at different rates and the method described in ref.[42] The maximum value of the current from each cycle was plotted against the square root of the scan rate, which derives from a

rearrangement of the Randles–Ševčík equation. The slope of this plot can be used to derive the Li^+ diffusion coefficient with the equation:

$$D = \left(\frac{Slope}{kAC}\right)^2 \qquad (E1)$$

where $k = 2.69\times10^5$ C mol^{-1} V$^{-1/2}$, A is the area of the electrode in cm^2 and C is the concentration of the Li^+ in mol cm^{-3}. The resulting linear fits have excellent R^2 values in the range 0.992 to 0.999. Figure 8c-d show the extracted diffusion coefficients are given in logarithmic form, to efficiently display the differences in orders of magnitude of the coefficients. It is worth noting that the diffusion coefficients are only properly defined for single-phase materials (*i.e.* it is impossible to predict the diffusion constant for two-phase materials given the complex interactions between the phases depending on morphology and phase distribution). The colored regions in figures 8c-d show the single-phase materials and these therefore also represents the regions where the diffusion constants are properly defined. In figure 8c it can be seen that the high loading electrodes yield very high D values (on the order of 10^{-6} cm^2 s^{-1}). By contrast, the low loading yields values nearly 2 orders of magnitude smaller. If anything, one would expect comparable or better diffusion in the thinner electrodes. However, in the Randles–Ševčík equation, A is the electrode area rather than the total area of contact between the electrode and electrolyte. In the high loading (about 20 mg cm^{-2}), the area contact is far larger than electrode area. We therefore recalculate D using an A value that is scaled with the mass loading of the electrodes (20/2.5 here) to correct this overestimation and yield results obtained for more common loadings used in the literature. The results are the black points in figures 8c,d. Interestingly, the overlap between the corrected high loading and the low loading results is nearly perfect. This has an important implication: the transport in our high loading combinatorial electrodes is not a limiting factor with these materials

(i.e., the transport in a 2.5 mg cm^{-2} is comparable to that in a much thicker 20 mg cm^{-2} electrode) and again demonstrates the potential of these materials.

The two binaries display similar diffusion coefficients with little change in the composition ranges of highest interest ($x, y > 0.5$). Little data concerning the diffusion coefficients of either binary have yet been discussed in the literature, however Griffiths *et al.* report Li diffusion constants from NMR results for Nb-W-O materials ranging from 1.1×10^{-9} cm^2 s^{-1} ($y = 0.529$) to 1.7×10^{-9} cm^2 s^{-1} ($y = 0.762$).[3,4] These values represent the self-diffusion coefficient and thus must be multiplied by the thermodynamic factor, Γ, to allow comparison to our values for the chemical diffusion coefficient. Landesfeind *et al.* determined that $\Gamma = 2.1$ for our electrolyte mixture.[44] This yields values of 2.3×10^{-9} cm^2 s^{-1} ($y = 0.529$) to 3.6×10^{-9} cm^2 s^{-1} ($y = 0.762$) for the chemical diffusion coefficient based on NMR. These values are lower than those obtained here by electrochemistry as one would expect given the above description of how the thickness of the electrodes impacts the extracted D value. Nonetheless, the results from Griffiths *et al.* does confirm the general increase of D with Nb content.

4. Conclusions

Newly developed high-throughput synthesis methods for high power anodes were used to study 63 compositions in two pseudobinary systems: $Nb_yW_{1-y}O_z$ and $Nb_xTi_{1-x}O_z$. They were characterized with XRD, and cyclic voltammetry. Of highest note from the structural point of view, large solid solutions were obtained in the $Nb_yW_{1-y}O_z$ system, despite a moderate sintering temperature used for synthesis.

Both binaries showed materials with high electrochemical performance, over very wide composition ranges. Generally speaking, quality anodes were obtained for all compositions with

Nb as at least 50 % of the metal atoms. High first cycle discharge capacities up to 235 mAh/g were obtained with low irreversible capacities. The $Nb_yW_{1-y}O_z$ binary featured more impressive capacity retentions of up to 96.8% after 10 cycles for some compositions while in the $Nb_xTi_{1-x}O_z$ binary the highest capacity retention found is 68.4 %. Both systems showed high rate performance, with some compositions retaining up to 96 % of their 0.1 V h^{-1} capacity at a sweep rate of 1 V h^{-1}. Analysis of the CVs at various rates allowed for the extraction of diffusion constants that again demonstrate high performance over very wide composition ranges (including 6 different phases, 5 of which exist as a solid solution in the phase stabilities).

The findings herein provide many insights of importance for the further development of these promising and challenging materials. Of note, correlating the electrochemical performance to the phase stability diagrams shows the rich chemistry available to make quality Nb-based materials by our combinatorial synthesis. This sets the stage to study both the Nb-Ti-W-O pseudoternary system and the impact of dopants in these materials.

Acknowledgements:

This work was funded by the Natural Sciences and Engineering Research Council of Canada under the auspices of a Discovery grant.

References

1 Y. Kim, Q. Jacquet, K. J. Griffith, J. Lee, S. Dey, B. L. D. Rinkel and C. P. Grey, *J. Electrochem. Soc.*, **168**, 10525 (2021).

2 S. Goriparti, E. Miele, F. De Angelis, E. Di Fabrizio, R. Proietti Zaccaria and C. Capiglia, *J. Power Sources*, **257**, 421–443 (2014).

3 K. J. Griffith, K. M. Wiaderek, G. Cibin, L. E. Marbella and C. P. Grey, *Nature*, **559**, 556–563 (2018).

4 K. Zhao, M. Pharr, J. J. Vlassak and Z. Suo, *J. Appl. Phys.*, **108**, 73517 (2010).

5 S. Rehman, S. Guo and Y. Hou, *Adv. Mater.*, **28**, 3167–3172 (2016).

6 A. S. Arico, P. Bruce, B. Scrosati, J.-M. Tarascon and W. Van Schalkwijk, *Mater. Sustain. Energy*, 148–159 (2010).

7 M. R. Palacín, P. Simon and J. M. Tarascon, *Acta Chim. Slov.*, **63**, 417–423 (2016).

8 V. Ganesh, A. Hunt and A. Faisal, *Mater. Matters*, **5**, 42–46 (2010).

9 S. Martinet, *Nanomaterials for rechargeable lithium batteries*, Springer Verlag, (2016).

10 M. Safari and C. Delacourt, *J. Electrochem. Soc.*, **158**, A1123 (2011).

11 S. J. An, J. Li, C. Daniel, D. Mohanty, S. Nagpure and D. L. Wood, *Carbon N. Y.*, **105**, 52–76 (2016).

12 Q. Shi, W. Liu, Q. Qu, T. Gao, Y. Wang, G. Liu, V. S. Battaglia and H. Zheng, *Carbon N. Y.*, **111**, 291–298 (2017).

13 M. Steinhauer, S. Risse, N. Wagner and K. A. Friedrich, *Electrochim. Acta*, **228**, 652–658 (2017).

14 Overdrive Battery Technology - InterStim Micro System | Medtronic, https://www.medtronic.com/us-en/healthcare-professionals/products/urology/sacral-neuromodulation-systems/interstim-micro/overdrive-battery-technology.html, (accessed 6 September 2022).

15 J. R. Harding, B. Han, S. B. Madden and Q. C. Horn, *Energies*, **15**, 1405 (2022).

16 W. Lv, J. Gu, Y. Niu, K. Wen and W. He, *J. Electrochem. Soc.*, **164**, A2213–A2224 (2017).

17 T. F. Yi, S. Y. Yang and Y. Xie, *J. Mater. Chem. A*, **3**, 5750–5777 (2015).

18 Y.-B. He, B. Li, M. Liu, C. Zhang, W. Lv, C. Yang, J. Li, H. Du, B. Zhang, Q.-H. Yang, J.-K. Kim and F. Kang, *Sci. Rep.*, **2**, 913 (2012).

19 I. Belharouak, G. M. Koenig, T. Tan, H. Yumoto, N. Ota and K. Amine, *J. Electrochem. Soc.*, **159**, A1165–A1170 (2012).

20 Y.-B. He, M. Liu, Z.-D. Huang, B. Zhang, Y. Yu, B. Li, F. Kang and J.-K. Kim, *J. Power Sources*, **239**, 269–276 (2013).

21 M. M. Thackeray and K. Amine, *Nat. Energy*, **6**, 683–683 (2021).

22 K. Zaghib, A. Mauger, H. Groult, J. B. Goodenough and C. M. Julien, *Materials (Basel).*, **6**, 1028–1049 (2013).

23 H. Yu, H. Lan, L. Yan, S. Qian, X. Cheng, H. Zhu, N. Long, M. Shui and J. Shu, *Nano Energy*, **38**, 109–117 (2017).

24 H. Ding, Z. Song, H. Zhang and X. Li, *Mater. Today Nano*, **11**, 100082 (2020).

25 R. S. Roth and J. L. Waring, *J. Res. Natl. Bur. Stand. Sect. A Phys. Chem.*, **70A**, 281 (1966).

26 J. L. Waring, R. S. Roth and H. S. Parker, *J. Res. Natl. Bur. Stand. Sect. A, Phys. Chem.*, **77A**, 705 (1973).

27 R. S. Roth, *Prog. Solid State Chem.*, **13**, 159–192 (1980).

28 E. McCalla, M. Parmaklis, S. Rehman, E. Anderson, S. Jia, A. Hebert, K. Potts, A. Jonderian, T. Adhikari and M. Adamič, *Can. J. Chem.*, **100**, 132–143 (2022).

29 K. P. Potts, E. Grignon and E. McCalla, *ACS Appl. Energy Mater.*, **2**, 8388–8393 (2019).

30 A. Jonderian, E. Anderson, R. Peng, P. Xu, S. Jia, V. Cozea and E. McCalla, *J. Electrochem. Soc.*, **169**, 50504 (2022).

31 T. Adhikari, A. Hebert, M. Adamič, J. Yao, K. Potts and E. McCalla, *ACS Comb. Sci.*, **22**, 311–318 (2020).

32 A. Jonderian, S. Jia, G. Yoon, V. T. Cozea, N. Z. Galabi, S. B. Ma and E. McCalla, *Adv. Energy Mater.*, 2201704 (2022).

33 M. D. Fleischauer, J. M. Topple and J. R. Dahn, *Electrochem. Solid-State Lett.*, **8**, A137 (2005).

34 V. K. Cumyn, M. D. Fleischauer, T. D. Hatchard and J. R. Dahn, *Electrochem. Solid-State Lett.*, **6**, E15 (2003).

35 H. J. Goldschmidt, *Met. Met. Form.***62** (1960).

36 G. H. de M. Gomes, R. R. d. Andrade and N. D. S. Mohallem, *Micron*, **148**, 103112 (2021).

37 C. G. Real, E. H. N. S. Thaines, L. A. Pocrifka, R. G. Freitas, G. Singh and H. Zanin, *J. Energy Storage*, **52**, 104793 (2022).

38 F. Holtzberg, A. Reisman, M. Berry and M. Berkenblit, *J. Am. Chem. Soc.*, **79**, 2039–2043 (1957).

39 A. Reisman, F. Holtzberg Vol, B. Arnold Reisman and F. Holtzberg, *J. Am. Chem. Soc.*, **81**, 3182–3184 (1959).

40 B. M. Gatehouse, A. D. Wadsl and : Ey, *Acta Crystallogr.*, **17**, 1545–1554 (1964).

41 Y. Yang, H. Zhu, J. Xiao, H. Geng, Y. Zhang, J. Zhao, G. Li, X.-L. Wang, C. Chao Li, Q. Liu, Y. Yang, J. F. Xiao, H. B. Geng, Y. F. Zhang, C. C. Li, H. Zhu, G. Li, X. Wang, Q. Liu and J. B. Zhao, *Adv. Mater.*, **32**, 1905295 (2020).

42 S. Jia, J. Counsell, M. Adamič, A. Jonderian and E. McCalla, *J. Mater. Chem. A*, **10**, 251–265 (2022).

43 M. Ritschel, H. Oppermann and N. Mattern, *Krist. und Tech.*, **13**, 1421–1429 (1978).

44 J. Landesfeind, A. Ehrl, M. Graf, W.A. Wall, and H.A. Gasteiger. *J. Electrochem. Soc.*, **163**, A1254 (2016).

Tables:

Table 1: Lattice parameters obtained from Pawley refinements of pure phase $Nb_yW_{1-y}O_z$ and $Nb_xTi_{1-x}O_z$ XRD patterns.

Material	Phase	Lattice parameters			
		a (Å)	*b* (Å)	*c* (Å)	*β* (°)
ICCD: 99-005-4222	WO_3	7.3010	7.5390	10.5211	133.22
y = 0	WO_3	7.303(8)	7.538(9)	10.52(1)	133.08(5)
ICDD: 99-001-5446	$Nb_{13.5}W_{20.5}O_{94}$	12.251	36.621	3.9430	90
y = 0.349	$Nb_{13.5}W_{20.5}O_{94}$	12.25(2)	36.62(6)	3.943(1)	90
y = 0.380	$Nb_{13.5}W_{20.5}O_{94}$	12.12(4)	36.6(1)	3.917(8)	90
y = 0.412	$Nb_{13.5}W_{20.5}O_{94}$	12.15(2)	36.62(6)	3.915(7)	90
y = 0.444	$Nb_{13.5}W_{20.5}O_{94}$	12.21(4)	36.6(1)	3.935(6)	90
y = 0.476	$Nb_{13.5}W_{20.5}O_{94}$	12.20(2)	36.62(6)	3.933(4)	90
y = 0.507	$Nb_{13.5}W_{20.5}O_{94}$	12.25(3)	36.62(9)	3.943(6)	90
y = 0.539	$Nb_{13.5}W_{20.5}O_{94}$	12.25(4)	36.6(1)	3.943(7)	90
y = 0.571	$Nb_{13.5}W_{20.5}O_{94}$	12.25(3)	36.62(9)	3.943(5)	90
y = 0.603	$Nb_{13.5}W_{20.5}O_{94}$	12.25(3)	36.62(9)	3.943(6)	90
y = 0.634	$Nb_{13.5}W_{20.5}O_{94}$	12.25(4)	36.6(1)	3.943(7)	90
y = 0.666	$Nb_{13.5}W_{20.5}O_{94}$	12.25(4)	36.6(1)	3.943(6)	90
ICDD: 99-001-0769	Nb_2WO_8	3.9490	17.622	16.626	90
y = 0.682	Nb_2WO_8	3.951(6)	17.61(3)	16.62(2)	90
y = 0.698	Nb_2WO_8	3.945(7)	17.60(3)	16.61(3)	90
y = 0.714	Nb_2WO_8	3.951(2)	17.62(1)	16.62(1)	90
y = 0.730	Nb_2WO_8	3.953(1)	17.63(7)	16.63(5)	90
ICDD: 99-001-5141	$Nb_{14}W_3O_{44}$	21.020	21.020	3.8240	90

y = 0.825	$Nb_{14}W_3O_{44}$	20.92(3)	20.92(3)	3.824(6)	90
y = 0.841	$Nb_{14}W_3O_{44}$	21.02(2)	21.02(2)	3.824(5)	90
y = 0.857	$Nb_{14}W_3O_{44}$	20.90(2)	20.90(2)	3.824(5)	90
Ref.[40]	Nb_2O_5	21.200	3.822	19.35	119.50
y = 0.984	Nb_2O_5	21.15(2)	3.815(2)	19.36(1)	119.77(4)
x = y = 1	Nb_2O_5	21.15(1)	3.816(2)	19.35(1)	119.64(3)
ICDD: 99-002-1294	TiO_2	4.6020	4.6020	2.9560	90
x = 0	TiO_2	4.593(3)	4.602(1)	2.960(3)	90
ICDD: 99-013-7910	Nb_2TiO_7	20.3699	3.8010	11.892	120
x = 0.698	Nb_2TiO_7	20.36(3)	3.801(1)	11.89(1)	120
ICDD: 99-011-8112	$Nb_{10}Ti_2O_{29}$	20.540	3.8140	15.540	113.683
x = 0.825	$Nb_{10}Ti_2O_{29}$	20.51(5)	3.810(7)	15.58(4)	113.43(2)
x = 0.857	$Nb_{10}Ti_2O_{29}$	20.53(4)	3.812(7)	15.57(3)	113.37(1)

Figures:

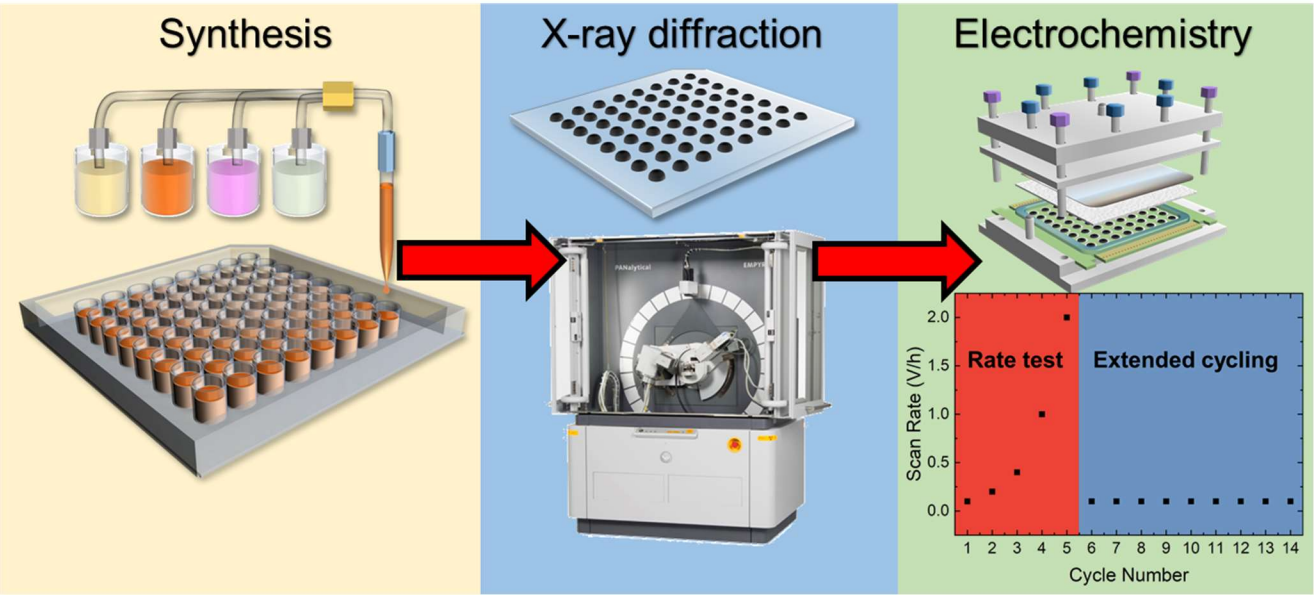

Figure 1: Schematic of the workflow used in this study.

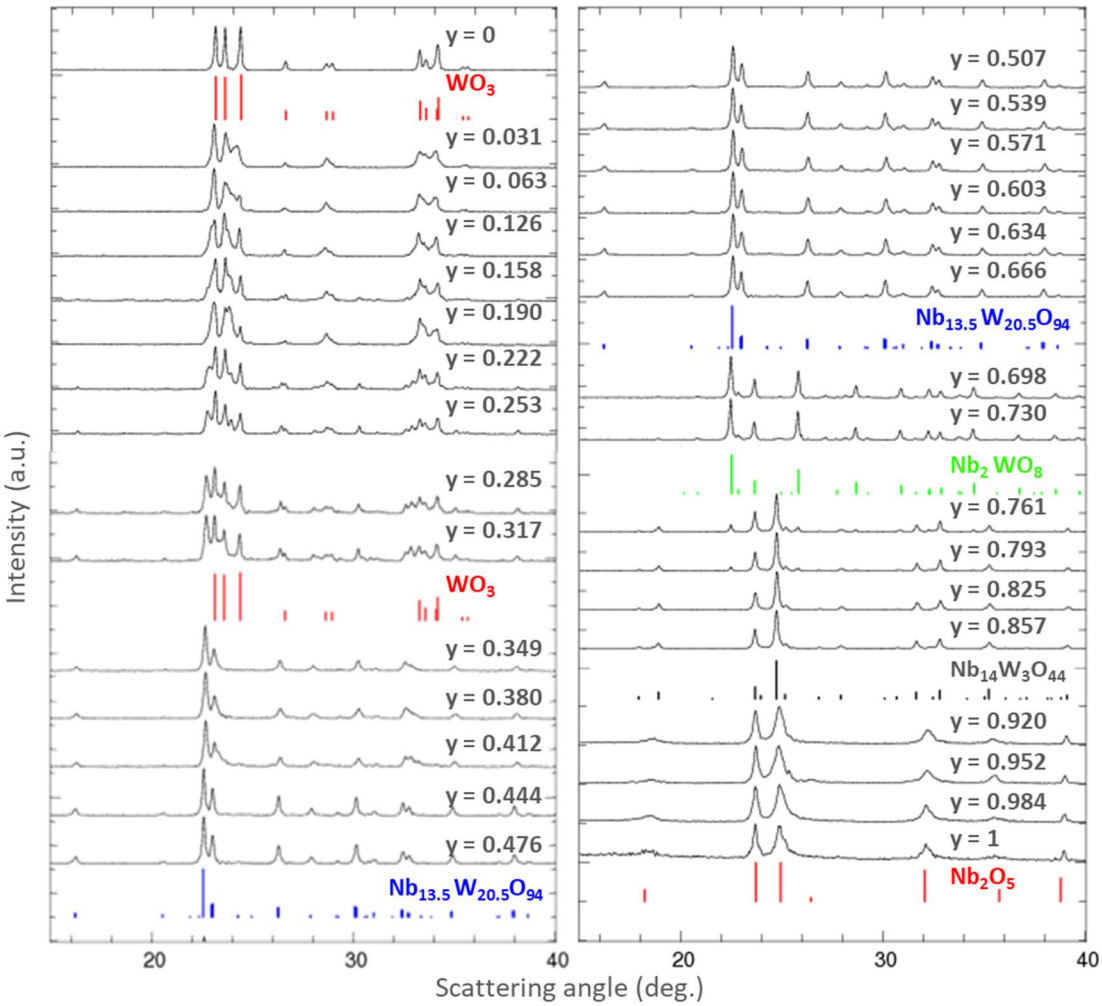

Figure 2: 32 XRD patterns along the $Nb_yW_{1-y}O_z$ pseudobinary composition line. Reference patterns used for phase identification and generation of the phase stability diagram are shown in color. The reference patterns are for ICDD numbers: 99-005-4222 (WO_3), 99-001-5446 ($Nb_{13.5}W_{20.5}O_{94}$), 99-001-0769 (Nb_2WO_8), 99-001-5141 ($Nb_{14}W_3O_{44}$). The Nb_2O_5 reference pattern is from ref.[43].

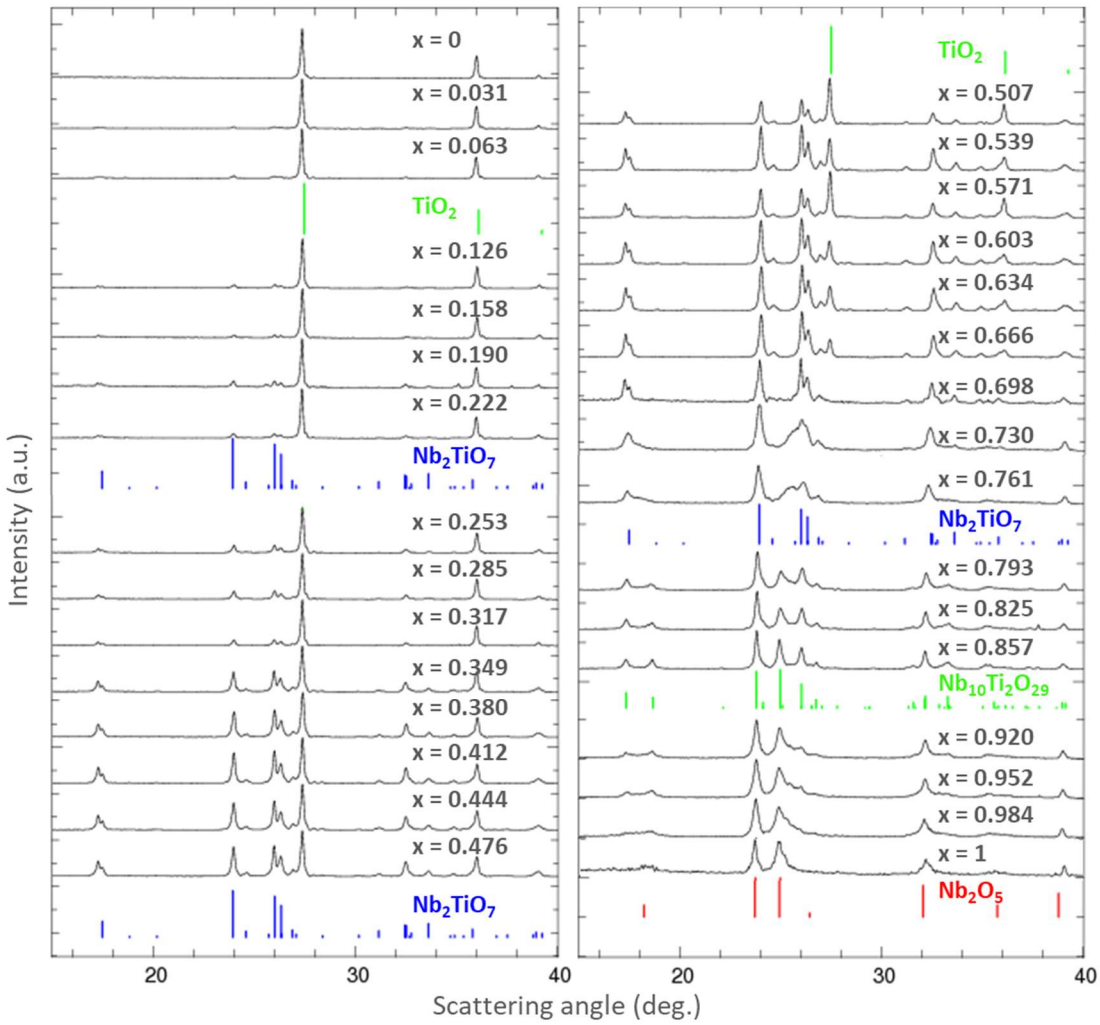

Figure 3: 32 XRD patterns along the $Nb_xTi_{1-x}O_z$ pseudobinary composition line. Reference patterns used for phase identification and generation of the phase stability diagram are shown in color. The reference patterns are for ICDD numbers: 99-002-1294 (TiO_2), 99-013-7910 (Nb_2TiO_7), 99-011-8112 ($Nb_{10}Ti_2O_{29}$). The Nb_2O_5 reference pattern is from ref.[43].

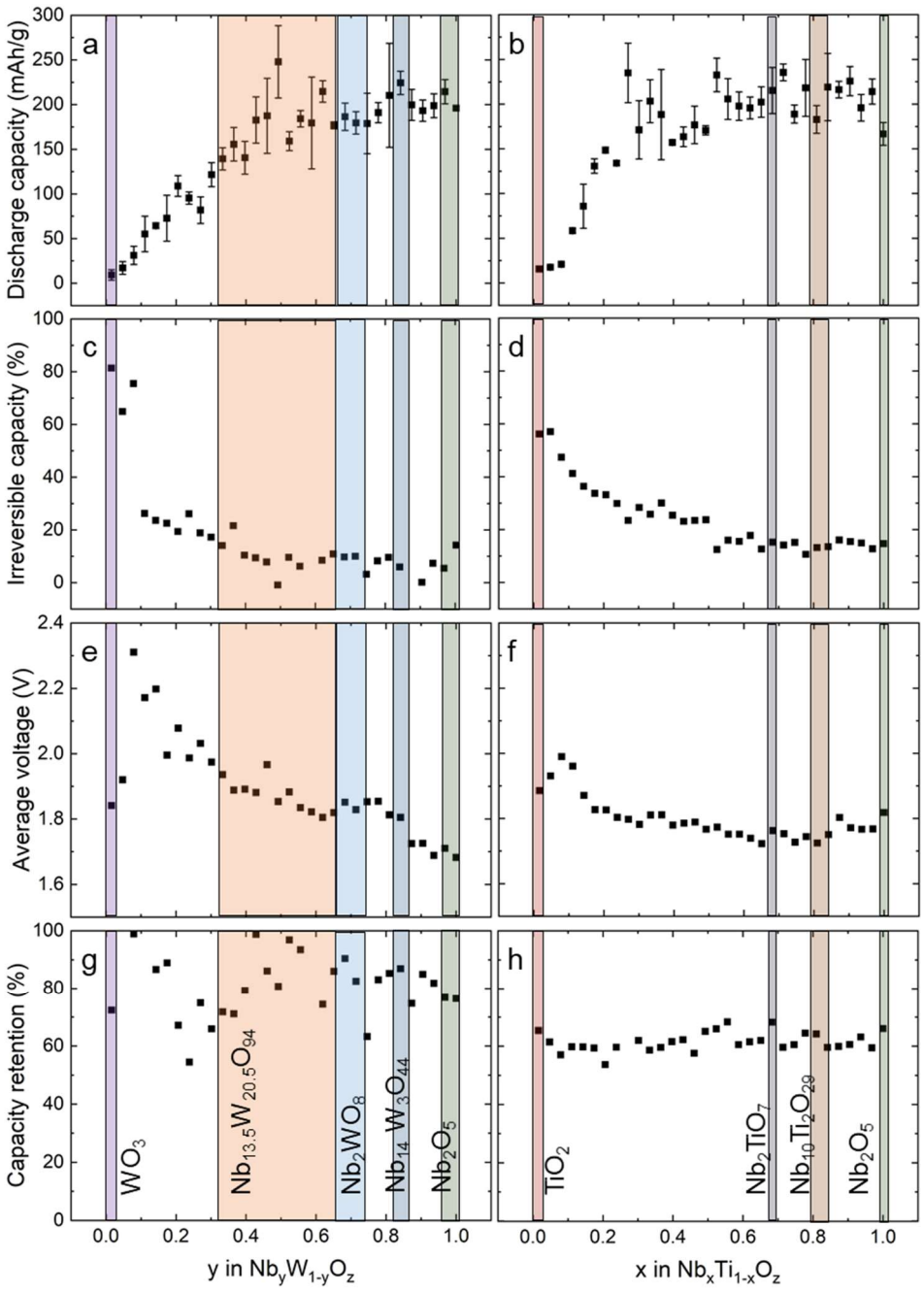

Figure 4: First discharge capacities of the a) $Nb_yW_{1-y}O_z$ and b) $Nb_xTi_{1-x}O_z$ binaries. Colored regions represent single-phase materials according to the XRD analysis with phase labels in panels g,h. Both materials show an increase in capacity with Nb content until a plateau around x,y = 0.5 Irreversible capacities are shown for the c) $Nb_yW_{1-y}O_z$ and d) the $Nb_xTi_{1-x}O_z$ binaries. Average cycling voltage for the e) $Nb_yW_{1-y}O_z$ and f) the $Nb_xTi_{1-x}O_z$ binaries showing a decrease in voltage with an increase in Nb content. Capacity retention after 10 cycles at 0.1 V h-1 for g) $Nb_yW_{1-y}O_z$ and h) $Nb_xTi_{1-x}O_z$ binaries show that both binaries do not vary much with composition.

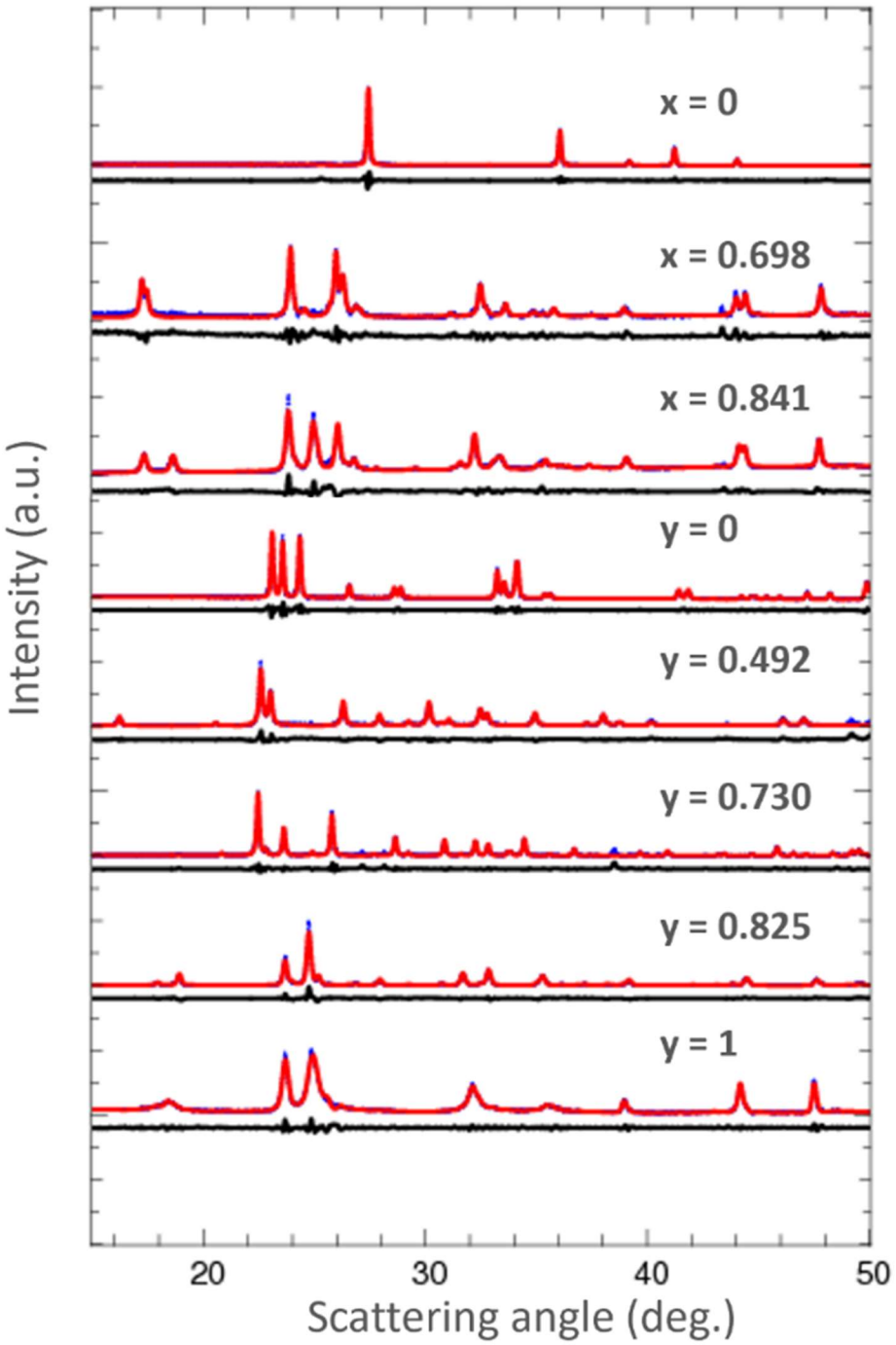

Figure 5: Representative fits of single-phase XRD patterns in both binaries. These represent single phase patterns for each of the phases shown in the phase stabilities. Lattice parameters for each fit are included in Table I.

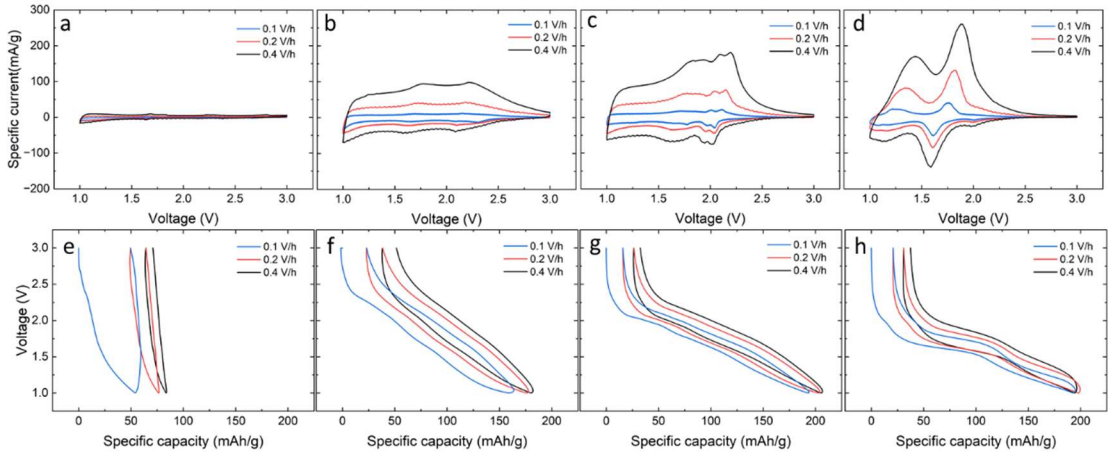

Figure 6: Representative CV profiles and corresponding voltage curves of the $Nb_yW_{1-y}O_z$ binary of several scan rates with compositions of y = 0.0158 (a,e), 0.349 (b,f), 0.555 (c,g), 0.984 (d,h), showing an increase in electrochemical activity with an increase in Nb content. All voltages are vs Li/Li^+

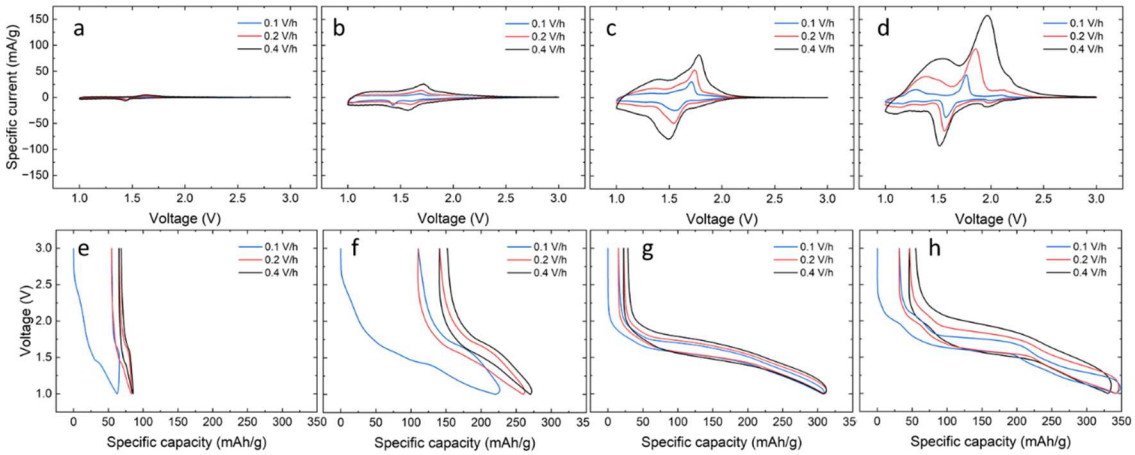

Figure 7: Titanium Representative CV profiles of the $Nb_xTi_{1-x}O_z$ binary of several scan rates with compositions of x= 0.0 (a,e), 0.237 (b,f), 0.666 (c,g), 1.0 (d,h), showing an increase in electrochemical activity with an increase in Nb content. All voltages are vs Li/Li^+.

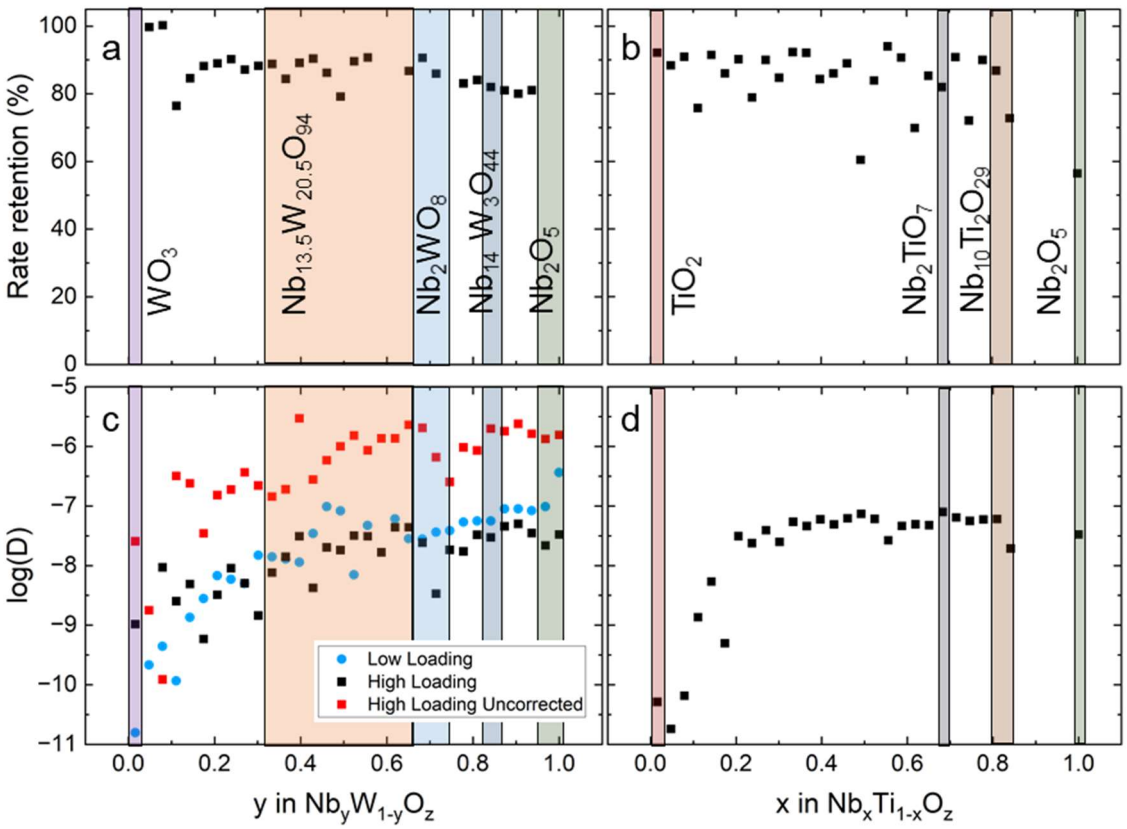

Figure 8: Rate retention (discharge capacity at 1 V h^{-1} divided by the capacity at 0.1 V h^{-1}) for both pseudobinaries (a,b). Logarithm of diffusion coefficients in cm^2 s^{-1} determined by cycling at different rates for both binaries (c,d).